remote sensing

MDPI

Article

Routine Processing and Automatic Detection of Volcanic Ground Deformation Using Sentinel-1 InSAR Data: Insights from African Volcanoes

Fabien Albino [1,*], Juliet Biggs [2], Milan Lazecký [3] and Yasser Maghsoudi [3]

[1] Univ. Grenoble Alpes, Univ. Savoie Mont Blanc, CNRS, IRD, Univ. Gustave Eiffel, ISTerre, 38000 Grenoble, France
[2] COMET, School of Earth Sciences, University of Bristol, Bristol BS8 1TH, UK
[3] COMET, School of Earth and Environment, University of Leeds, Leeds LS2 9JT, UK
* Correspondence: fabien.albino@univ-grenoble-alpes.fr

Abstract: Since the launch of Sentinel-1 mission, automated processing systems have been developed for near real-time monitoring of ground deformation signals. Here, we perform a regional analysis of 5 years over 64 volcanic centres located along the East African Rift System (EARS). We show that the correction of atmospheric signals for the arid and low-elevation EARS volcanoes is less important than for other volcanic environments. We find that the amplitude of the cumulative displacements exceeds three times the temporal noise of the time series (3σ) for 16 of the 64 volcanoes, which includes previously reported deformation signals, and two new ones at Paka and Silali volcanoes. From a 5-year times series, uncertainties in rates of deformation are ~0.1 cm/yr, whereas uncertainties associated with the choice of reference pixel are typically 0.3–0.6 cm/yr. We fit the time series using simple functional forms and classify seven of the volcano time series as 'linear', six as 'sigmoidal' and three as 'hybrid', enabling us to discriminate between steady deformation and short-term pulses of deformation. This study provides a framework for routine volcano monitoring using InSAR on a continental scale. Here, we focus on Sentinel-1 data from the EARS, but the framework could be expanded to include other satellite systems or global coverage.

Keywords: Sentinel-1 SAR; volcanic ground deformation; East Africa

check for updates

Citation: Albino, F.; Biggs, J.; Lazecký, M.; Maghsoudi, Y. Routine Processing and Automatic Detection of Volcanic Ground Deformation Using Sentinel-1 InSAR Data: Insights from African Volcanoes. *Remote Sens.* **2022**, *14*, 5703. https://doi.org/10.3390/rs14225703

Academic Editor: Alessandro Bonforte

Received: 12 September 2022
Accepted: 26 October 2022
Published: 11 November 2022

Publisher's Note: MDPI stays neutral with regard to jurisdictional claims in published maps and institutional affiliations.

Copyright: © 2022 by the authors. Licensee MDPI, Basel, Switzerland. This article is an open access article distributed under the terms and conditions of the Creative Commons Attribution (CC BY) license (https://creativecommons.org/licenses/by/4.0/).

1. Introduction

Interferometric Synthetic Aperture Radar (InSAR) can routinely produce ground displacement maps over large areas. Current satellite missions, especially Sentinel-1, are well-suited for carrying out deformation surveys on the scale of entire plate boundaries, which would not be feasible with ground-based stations. Previous large-scale surveys have mostly been retrospective analyses of strain accumulation in tectonically active regions such as Tibet [1] and Anatolia [2,3], and surveys of volcanic unrest [4–9].

The availability of SAR datasets has increased dramatically over the past decade. In particular, the open-access policy of the Sentinel-1 mission opened new perspectives for the near real-time monitoring of ground deformation at global and regional scales [3,9–11]. This has been supported by the development of automated processing platforms that now produce large databases of InSAR products: ARIA (NASA Jet Propulsion Laboratory), SARVIEWS (University of Alaska Fairbanks), Geohazards Exploitation Platform (European Space Agency), and LiCSAR (COMET) [12–15].

Satellite observations are particularly critical for sub-saharan Africa, where the resources to deploy and maintain a dense network of ground-based stations are limited. The East African Rift System (EARS) contains 78 volcanoes considered active during Holocene [16]. Population exposure is high, particularly in Ethiopia and Kenya, where over 70 million people live within a 100 km radius of a Holocene volcano [17]. InSAR

regional surveys using the ERS (1997–2000) and ENVISAT (2003–2010), satellites improved our knowledge of the dynamics of the EARS magmatic systems [7,8]. However, these early missions were not designed for continuous monitoring, and the dataset had low temporal resolution (3–4 images per year) and many gaps. More recently, [9] analysed Sentinel-1 data over 64 Holocene active volcanoes along the EARS between October 2014 and January 2020 and detected ground deformation signals at 14 volcanic centres.

Here, we discuss the best practices for using Sentinel-1 SAR data for the automatic production of time series and the characterisation of volcanic ground deformation signals, using the EARS as a case study (Figure 1). First, we describe the methodological developments that support the routine production of Sentinel-1 InSAR time series. We then analyse the 64 EARS volcanoes to assess the benefit of atmospheric corrections for rift volcanoes and estimate the uncertainties on the mean line-of-sight (LOS) velocities. We apply a threshold based on the noise level at each volcano to detect deformation and classify the resulting time-series using simple functional forms. Finally, we discuss the implications for this regional study for global volcano monitoring, in terms of the limits of detection and classification.

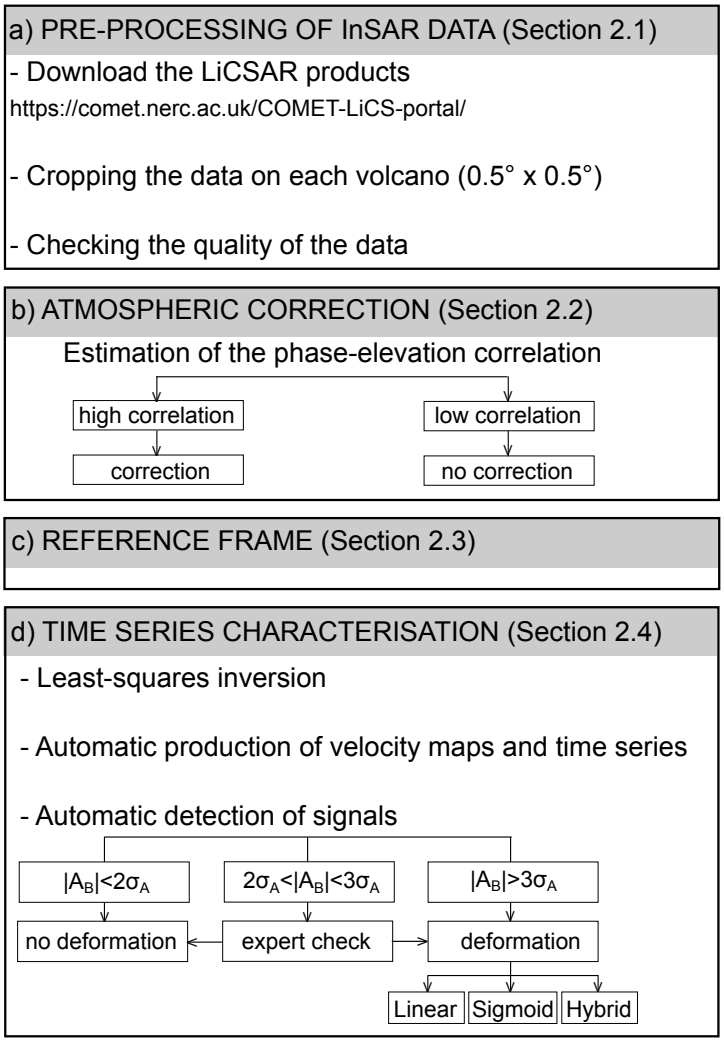

Figure 1. Flowchart showing the important steps for the automatic production and classification of Sentinel-1 time series.

2. Materials and Methods

In this section, we describe the methods used for the automated processing and classification of Sentinel-1 data over the 64 volcanoes of the EARS (Figure 1). We start by

describing the processing of the Sentinel-1 data, and our approach to atmospheric corrections and reference frame selection. We then describe the methods used to analyse the set of time-series, including the automatic detection and classification of deformation signals.

2.1. Pre-Processing of Sentinel-1 Data

Sentinel-1 is a C-band imaging radar mission operated by the European Satellite Agency (ESA) through the Copernicus programme. The constellation consists of two satellites: Sentinel-1A (launched 3 April 2014) and Sentinel-1B (launched 25 April 2016). However, an anomaly occurred on Sentinel-1B satellite on 23 December 2021 and the end of the Sentinel-1B mission was announced by ESA and the European Commission on August 2022. In Africa, revisit time of Sentinel-1 acquisitions is 12 days during the 2017–2021 period and 24 days otherwise. Differential Interferometric Synthetic Aperture Radar (DInSAR) consists of computing the phase difference between two SAR images of the same geographical location acquired at different times [18]. The processing of SAR images produces (i) wrapped interferograms which contain ambiguous phase values between $-\pi$ and π, (ii) unwrapped interferograms which contain continuous phase values relative to a reference pixel and (iii) coherence maps, which indicate the degree of decorrelation of ground targets.

We generate Sentinel-1 interferograms and coherence maps using the LiCSAR processing system [15], which is built on the GAMMA software package [19] (Figure 1a) . Our dataset spans a 5-year period (2015–2020) and consists of a total of 3570 interferograms covering 64 Holocene active volcanoes from the Eastern Branch of the African Rift system, including Ethiopia, Kenya and Tanzania (Table S1). All InSAR products are freely available at https://comet.nerc.ac.uk/comet-lics-portal/ (accessed on 25 October 2022). The LiCSAR system automatically generates the 3–4 shortest temporal baseline interferograms at a spatial resolution of 0.001° (∼111 m at the equator) [15]. To reduce the computing time for the time series analysis, we first crop all the LiCSAR products to a geographical region 0.5° × 0.5° centred on the location of each volcano derived from the Smithsonian catalogue [16] (Figure 1a) .

A small proportion of the automatically-generated interferograms have poor quality due to processing issues (e.g., missing data, co-registration errors) or limitations of the InSAR method (e.g., temporal decorrelation). We apply a quality test based on two criteria calculated on the cropped area: (1) the mean coherence and (2) the fraction of pixels unwrapped (Figure 1a). We select images with average coherence exceeding 0.05 and the fraction of pixels unwrapped exceeding 0.2. The aim is to remove images that contain no information due to issues in the processing. For example, among the 294 total interferograms processed at Fentale volcano, only six did not pass the quality test (Figure S1 in Supplementary Materials). For the total dataset, the proportion of rejected interferograms is <8% (Figure S2 in Supplementary Materials).

2.2. Atmospheric Noise

Changes in the atmospheric conditions (mostly pressure and water vapour) between two SAR acquisitions cause phase delays in an interferogram that can potentially mask real ground deformation signals. The impact of these atmospheric signals is expected to be most significant for InSAR measurements in regions with high-relief, as large elevation gradients may cause strong stratified signals, and for regions located in tropical climates where large spatio-temporal variations of water vapour content may induce turbulent signals. Topographically-correlated atmospheric signals have been identified at many high-elevation stratovolcanoes, including arc volcanoes located in tropical regions such as Central America and Indonesia [20–22] and continental volcanoes such as Etna (Italy) and Hasan Dagi (Turkey) [23,24]. These topography-dependent signals can be reduced using (1) empirical methods based on the correlation between phase and elevation [23,25,26] and (2) weather-based models [22,27–30], which have the ability to correct both topographically-correlated and long-wavelength turbulent components.

Although much of the EARS is located in the tropics, most of the volcanoes are low relief and lie in desert and semi-arid climates [31]. More than 80% of the EARS volcanoes have relief <1000 m, with height average value of ∼690 m in Afar, ∼340 m in the Main Ethiopian Rift (MER) and ∼650 m in the Tanzania-Kenya rift (Figure S3 in Supplementary Materials). Previous InSAR studies have reported no obvious atmospheric errors in the MER and Kenya-Tanzania rift [8,32] whereas significant atmospheric noise has been reported in the Afar region [33,34].

We calculate the coefficient of determination, R^2, between the interferometric phase and the elevation for each of the >4000 unwrapped interferograms processed (Figure 1b). For each volcano, we then calculate the cumulative distribution function (CDF) of the R^2 values for each region (Figure 2a–c). CDF curves located close to the top-left corner of the plot correspond to volcanoes that typically present a low phase-elevation correlation while CDF curves that plot close to the diagonal correspond to volcanoes with a uniform distribution of R^2 values.

2.3. Reference Frame

Differential interferometry measures relative displacement, meaning the choice of reference frame has an influence on the time-series and velocity estimates. Possible choices for the reference value include: (i) a single pixel or an average of a region [27,35] located far from the deformation area and coherent in time, (ii) the average value of each unwrapped interferogram [36], (iii) the average of an annulus centred on the volcano summit [20], (iv) the evaluation of all pixels outside the volcanic area as a potential reference [21].

The first approach is based on an arbitrary choice. The second one is based on the assumption of zero mean deformation, which is not appropriated for volcanic areas with potential long-lived surface deformation. The third approach was designed for volcanoes in order to reduce the effect of small-scale atmospheric variations on the time series. However, the method only works for symmetrical edifices with a clearly-identified summit (e.g., stratovolcanoes, cones) and is not suitable for many of the volcanic centres located in the East African Rift.

For these reasons, we chose the method developed by [21] as it provides several advantages for our study: it is well-suited for automation, it minimises the effects of local atmospheric artefacts and it provides an estimate of the associated uncertainty (Figure 1c). We consider all pixels located more than 20 km from the volcano summit as a potential reference pixel to ensure that those are not affected by any ground deformation. Then, we derive the distribution of the corresponding LOS velocity estimates at the centre of the volcano. We select a pixel associated with the peak of the distribution as the reference point. The standard deviation of this distribution, σ_{ref}, is a measure of the uncertainty in the LOS velocity estimate, and we will henceforth refer to it as the 'reference uncertainty'.

2.4. Time Series Characterisation

We produce time series of ground displacements using the classic least-squares approach [35,37] with no temporal filtering applied (Figure 1d). For each volcano, time series are automatically generated at two specific points: (i) the point A, chosen outside the volcanic area and (ii) the point B corresponding to the location where cumulative displacements are maximum in the volcanic area (Figure S4 in Supplementary Materials). For each volcano, we calculate (1) the temporal standard deviation of the time series at the point A, σ_A, which characterises the noise level and (2) the modulus of the cumulative LOS displacement at the point B, $|A_B|$, which characterises the amplitude of the signal (Figure 1d).

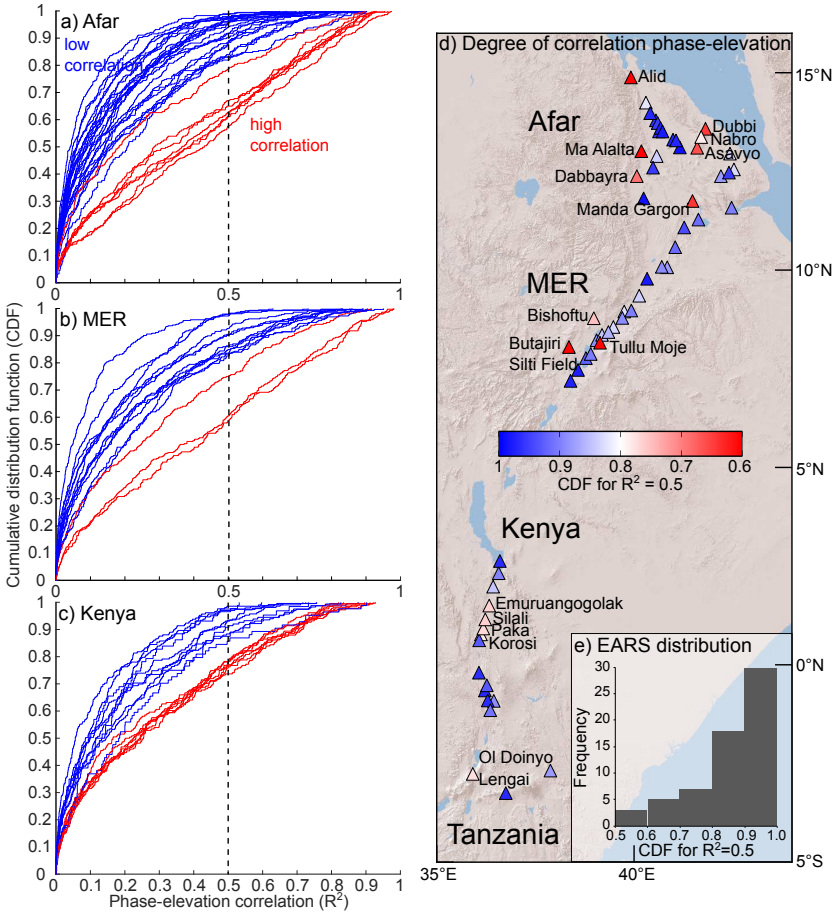

Figure 2. Cumulative Distribution Function (CDF) of the phase-elevation correlation values (R^2) recorded for each volcano at different location along the rift: (**a**) Afar, (**b**) Main Ethiopia Rift, and (**c**) Kenya-Tanzania. Blue lines indicate volcanoes with low phase-elevation correlation (CDF(0.5) $>$ 0.8) and red lines indicate volcanoes with high phase-elevation correlation (CDF(0.5) $<$ 0.8), (**d**) map showing the degree of phase-elevation correlation through the value CDF(0.5) for all the volcanoes processed. All volcanoes showed with red triangles were corrected using phase-elevation correlation, (**e**) distribution of the phase-elevation correlation along the EARS.

2.4.1. Time Series Functions

For those volcanoes showing deformation signals, we fit the time series, $U(t)$ in the point B by using two simple models: a linear function to represent steady-state deformation and a sigmoid function to represent transient deformation. These are not intended to reflect the underlying geophysical processes but are a simple way to parametrize and compare a range of signals (Figure 1d) . The functions are chosen to have a small number of unknown parameters (2–3) and the ability to approximate a range of behaviours

The linear function, $U(t) = vt + U(0)$, has two parameters with v corresponding to the mean velocity. The sigmoid function

$$U(t) = \frac{U_{max}}{1 + e^{-(\frac{t-t_c}{\tau})}} \quad (1)$$

has three parameters: U_{max}, the maximum displacement at $t = \infty$, τ is the characteristic time and t_c is the time at the centre of the sigmoid. We consider the time period between $t = t_c - 2\tau$ and $t = t_c + 2\tau$, which contains 76% of the total displacements U_{max}, as a proxy of the period of unrest.

For each time series, we calculate the R^2 for the linear and sigmoid functions. For those time series where both linear and sigmoid models provide an acceptable fit ($R^2 > 0.5$),

we then use Akaike's Information Criterion (AIC) [38] to compare the goodness of fit while accounting for the different number of model parameters. Since AIC is a relative measure, we quote the value $\Delta AIC = AIC_{sigmoid} - AIC_{linear}$ and assume that the errors have independent identical normal distributions, such that

$$\Delta AIC = (n \ln \frac{RSS_s}{n} + 2k_s) - (n \ln \frac{RSS_l}{n} + 2k_l) \quad (2)$$

where n is the number of data in the time series, RSS is the residual sum of squares, and k is the number of model parameters. The subscripts l and s correspond to the linear and sigmoidal models, respectively. Here, $k_l = 2$ and $k_s = 3$, the expression can be simplified as:

$$\Delta AIC = n(\ln \frac{RSS_s}{RSS_l}) + 2 \quad (3)$$

If $\Delta AIC << 0$, the best model is the sigmoid and, if $\Delta AIC >> 0$, the best model is linear. For $-10 < \Delta AIC < 10$, the two models are roughly equivalent, and we select the linear model for simplicity.

2.4.2. Velocity Uncertainties

We then evaluate the LOS velocity uncertainties in the Sentinel-1 time series for our EARS dataset by looking at the time series for the volcanoes that show a continuous linear trend. The standard deviation of the LOS velocity is derived using the percentile bootstrap method [39]. The method consists of computing the distribution of the velocity using a random selection of N resampled datasets with data replacement (here, we chose N = 100). The standard deviation of the velocity is then calculated for different duration from 1 to 5 years.

Regional and global analysis of geodetic time series have showed that velocity uncertainties σ_v decrease with the duration of the time series Δt, following a power-law function $\sigma_v = \Delta t^{-b}$ [40–42]. The parameter b corresponds to the decay rate, and it usually ranges between 1 for flicker noise (correlated) and $\frac{3}{2}$ for pure white noise (uncorrelated). For two previous studies using Sentinel-1 InSAR dataset, such power-law relationships have been modelled with a decay rate corresponding to white noise ($b = \frac{3}{2}$) [3,43].

3. Results

3.1. Atmospheric and Reference Frame Uncertainties

The EARS volcano dataset shows a low correlation between elevation and the phase of the interferograms. We found that (i) the coefficient of determination, R^2, has an average value of 0.2 and (ii) only 15% of the interferograms processed show a $R^2 > 0.5$. As an illustration, Figure 3a shows one interferogram containing a strong stratified signal from Silali volcano. An empirical model based on the linear correlation between phase and elevation (R^2 = 0.8) largely removes the atmospheric signal (Figure 3b,d) and the residuals after correction have a standard deviation of <2 cm (Figure 3c). Figure 3e shows one interferogram containing low atmospheric signal from Suswa volcano. Here, the empirical model based on the phase-elevation correlation (R^2 = 0.04) does not improve the quality of the data (Figure 3f,h) and the corrected interferogram is very similar to the original interferogram (Figure 3g).

To avoid over-correcting any real deformation signals, we only apply the empirical phase-elevation corrections at volcanoes for which many interferograms show high correlation. We chose to apply phase-elevation corrections at volcanoes for which more than 20% of interferograms have a correlation coefficient larger than 0.5 [CDF(R^2 = 0.5) < 0.8] (Figure 2a,c—red lines). This corresponds to only 15 of the 64 volcanoes processed (23%) (Figure 2d,e): seven volcanoes in Afar (Alid, Ma-Alalta, Dabbayra, Manda-Gargori, Asavyo, Nabro and Dubbi), three in the Main Ethiopian Rift (Bishoftu, Butajiri-Silti field and Tullu Moye) and five in the Kenyan-Tanzania Rift (Emuruangogolak, Silali, Paka, Korosi and Ol

Doinyo Lengai). For Afar and the MER, we notice that the volcanoes that require corrections are mostly located at the margin of the rift (Figure 2d), where the relief of the border faults rather than the topography of the volcanic edifice generates the topographically-correlated signal. Our statistic analysis confirms that atmospheric noise is generally low for the EARS volcanoes and consequently atmospheric corrections are not a critical step for the detection of volcanic ground deformation signals.

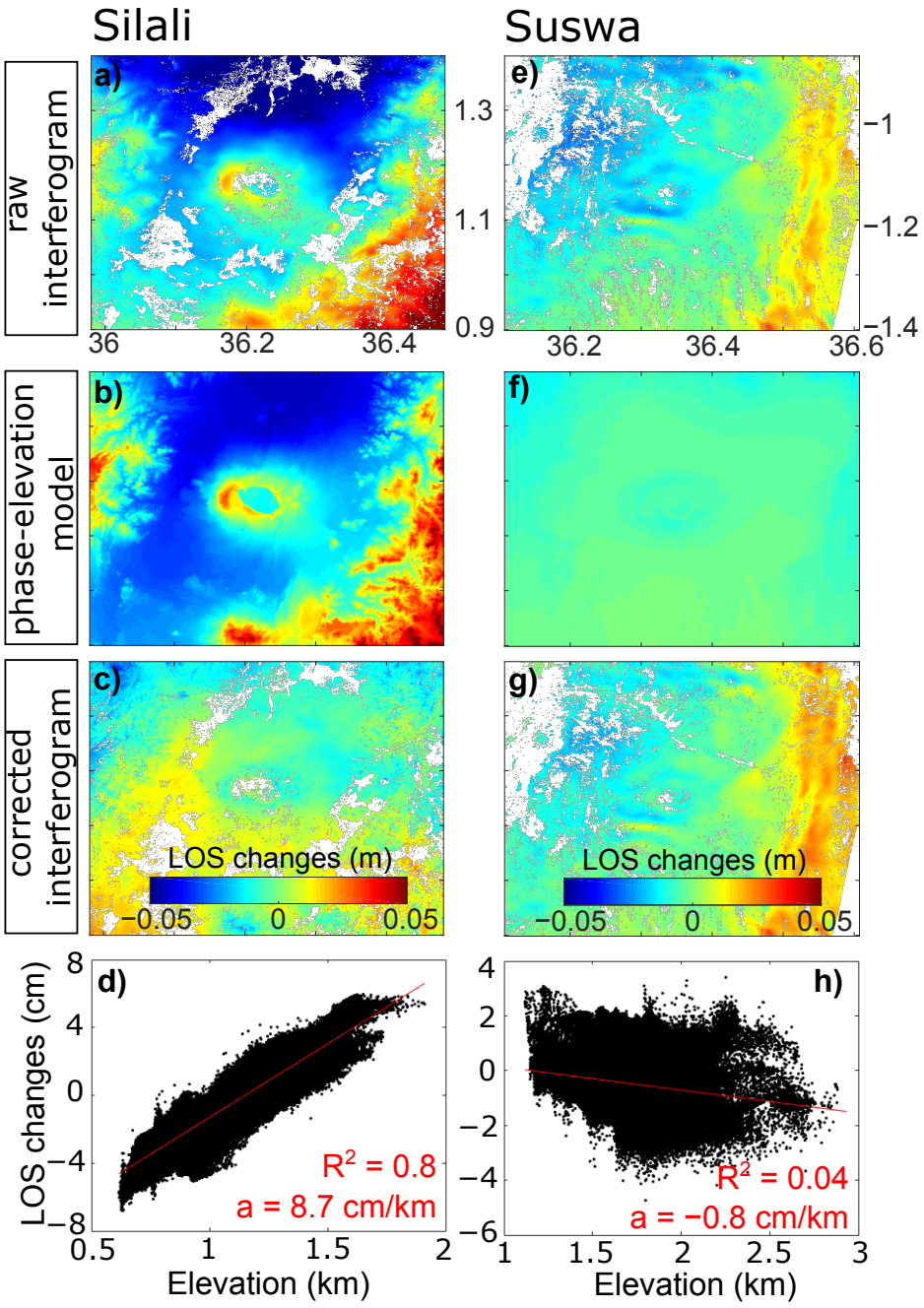

Figure 3. Atmospheric corrections using the empirical method of linear phase-elevation correlation. The top row shows an example for Silali volcano showing high correlation (R^2 = 0.8) with (**a**) the interferogram, (**b**) the phase-elevation model, (**c**) the corrected interferogram and (**d**) the phase-elevation plot. The bottom row shows an example for Suswa volcano showing low correlation (R^2 = 0.04) with (**e**) the interferogram, (**f**) the phase-elevation model, (**g**) the corrected interferograms and (**h**) the phase-elevation plot.

Reference frame uncertainties vary widely among the EARS volcanoes with values ranging between 0.18 cm/yr (Groppo) and 1.65 cm/yr (Gufa) with an average of ~0.5 cm/yr (Figure 4d, Tables S1–S3 in Supplementary Materials). Figure 4a–c shows example histograms from Dallol (0.4 cm/yr), Nabro (0.8 cm/yr) and South Island (1.6 cm/yr). Two thirds of the 64 EARS volcanoes studied have reference uncertainties between $0.3 < \sigma_{ref} < 0.6$ cm/yr. The four end-members (Alid, Gufa, South island and The Barrier) with reference uncertainties greater than 1 cm/yr (Figure 4e) are volcanoes that have the smallest number of interferograms processed (Figure S2 in Supplementary Materials).

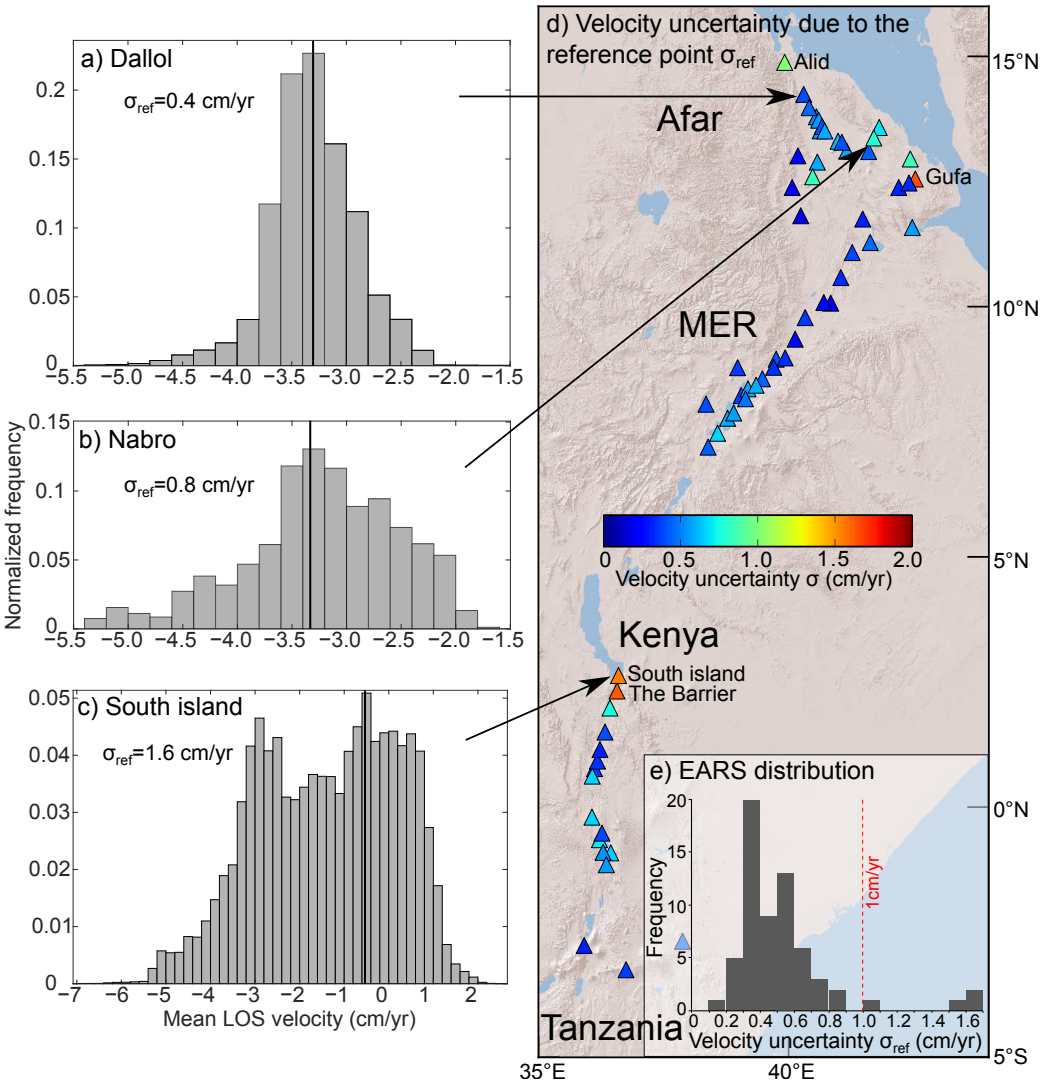

Figure 4. Distribution of the LOS velocity estimates at the centre of the volcanoes (**a**) Dallol, (**b**) Nabro and (**c**) South island, using all the pixels outside the volcanoes as a potential reference point. Vertical black lines indicate the peak of frequency. The standard deviation of the distribution (1σ) is an indication of the velocity uncertainty due to the choice of the reference point, (**d**) map showing the LOS velocity uncertainty for all the volcanoes processed, (**e**) distribution of the uncertainty along the EARS.

3.2. Analysis of Deformation Signals

3.2.1. Signal-to-Noise Ratio

We plot the amplitude of the signal ($|A_B|$) as a function of the temporal noise (σ_A) for each of the 64 volcanoes processed (Figure 5). The noise level σ_A is similar between the

three EARS regions, with mean values of 1.4 ± 0.5 cm, 1.2 ± 0.4 cm, and 1.4 ± 0.5 cm (1σ) for Afar, MER and Kenya-Tanzania, respectively (Table 1).

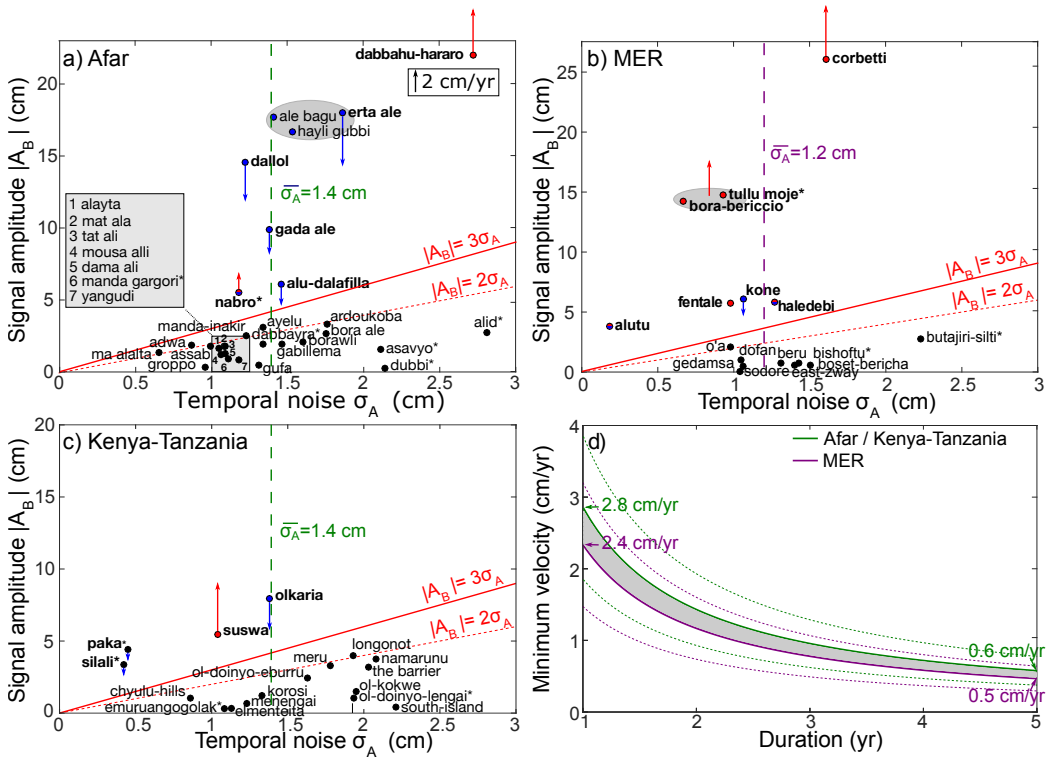

Figure 5. Limit of detection of displacements for the different sections of the rift: (**a**) Afar, (**b**) MER and (**c**) Kenya-Tanzania. The signal amplitude corresponds to the absolute value of the cumulative displacement recorded by the time series after 5-years at the location (B). Temporal noise corresponds to the standard deviation of the 5-years time series at the location (A) outside the deformation. The red lines show the two detection thresholds: $|A_B| = 2\sigma_A$ and $|A_B| = 3\sigma_A$. Volcanic centres with amplitude above $3\sigma_A$ are automatically classified as deformed volcanoes whereas volcanoes with amplitude between $2\sigma_A$ and $3\sigma_A$ need manual inspection. Arrows indicate the mean LOS velocity for the year 2019. Gray ellipse indicates cases for which one ground signal is identified on different neighboured volcanic centres. The symbol (*) indicates volcanic centres where phase-elevation corrections have been applied. Vertical dashed lines indicate the average temporal noise for each section of the rift, (**d**) minimum LOS velocity that will be detected as a function of the duration of the time series, assuming the threshold of $2\sigma_A$. Solid lines are derived from the mean value of the temporal noise found in (**a**–**c**) and dashed lines indicate the confidence intervals within 1 standard deviation.

For volcanoes which did not deform, the amplitude of the signal is the same order of magnitude as the noise level (e.g., Gedamsa: $|A_B|$ = 0.9 cm and σ_A = 1 cm) (Figure S4a–c in Supplementary Materials). For volcanoes that did deform, the amplitude of the signal is much higher than the temporal noise (e.g., Tullu Moje: $|A_B|$ = 14.7 cm and σ_A = 1 cm) (Figure S4d–f in Supplementary Materials).

We evaluate two threshold's values for the detection of volcanic unrest: $|A_B| = 2\sigma_A$ and $|A_B| = 3\sigma_A$. The amplitude $|A_B|$ exceeds $3\sigma_A$ for 19 volcanoes, which is ∼30% of the total number (Table 2; coloured circles in Figure 5). This includes eight volcanoes in Afar (Nabro, Alu-Dalafilla, Gada Ale, Dallol, Alu Bagu, Hayli Gubbi, Erta Ale and Dabbahu-Hararo), seven in the MER (Alutu, Fentale, Kone, Haledebi, Bora-Bericcio, Tullu Moje and Corbetti) and four in Kenya-Tanzania (Suswa, Olkaria, Paka and Silali). Three of these are actually duplicates, where two or more closely spaced volcanoes appear in the same 0.5° × 0.5° tile: the signal from Erta Ale also appears in the tiles for Alu Bagu and Hayli Gubbi and the signal from Tullu Moje also appears in the tile for Bora Bericcio. These duplicates are

removed from the subsequent analysis, leaving 16 unique signals. With the exception of Silali and Paka, all these signals were reported as ground deformation signals in Albino and Biggs [9].

As we decrease the threshold to $2\sigma_A$ (dashed line in Figure 5), five volcanoes will be flagged in addition to the 16 previously detected, with three in Afar (Ma Alalta, Adwa, Ayelu), one in the MER (O'a caldera) and one in Kenya-Tanzania (Longonot). The choice of the appropriate threshold is a compromise between the number of false alarms (if the threshold is too low) and the numbers of missed detections (if the threshold is too high). In our case, we suggest to automatically flag as deformation each signal with amplitude exceeding 3σ, and to manually inspect signals with amplitude between 2σ and 3σ (see Section 4).

Table 1. Statistical values (mean, median, standard deviation, minimum and maximum values) associated with the temporal noise σ_A for each of the three EARS regions (Afar, MER, Kenya-Tanzania). Units are in centimetres.

Region	Nb of Volc.	Mean	Median	Std	Min/Max
Afar	31	1.4	1.3	0.5	0.7/2.8
MER	16	1.2	1.1	0.4	0.2/2.2
Kenya-Tanzania	17	1.4	1.4	0.5	0.4/2.2

Table 2. Values of the signal-to-noise ratio and the best-fit model for InSAR time series of all volcanoes where $|A_B| > 3\sigma_A$.

Volcano	$\lvert A_B\rvert$ (cm)	Detection σ_A (cm)	$\lvert A_B\rvert/\sigma_A$	Model ΔAIC	Sigmoid t_c (Days)	$R^2 > 0.75$ τ (Days)	U_{max} (cm)
Fentale	5.8	1.0	5.8	−133	20150422	43	8.3
Erta Ale	18.0	1.9	9.5	−86	20170626	146	−19.0
Tullu Moje	14.7	1.0	14.7	−61	20161130	212	13.4
Suswa	5.5	1.0	5.5	−49	20181025	64	6.2
Kone	6.1	1.2	5.1	−31	20190329	426	−8.2
Olkaria	7.9	1.4	5.6	−10	20170429	261	−10.7
				Model ΔAIC	**Linear** v_B (cm/yr)	$R^2 > 0.75$ σ_B (cm/yr)	b
Corbetti	26.1	1.6	16.3	−4	4.6	0.1	1.47
Alu−Dallafilla	6.10	1.5	4.1	−3	−1.3	0.1	1.53
Silali	3.4	0.4	8.5	−2	−0.7	0.05	1.35
Dallol	14.6	1.2	12.2	10	−3.2	0.1	1.45
Paka	4.4	0.5	8.8	11	−0.7	0.06	1.61
Gada Ale	9.9	1.4	7.1	21	−1.9	0.1	1.45
Dabbahu	22.0	2.7	8.1	23	3.9	0.2	1.65
				Model	**Linear** v_B (cm/yr)	**+ Seasonal** A_s (cm)	
Nabro	5.5	1.2	4.6		1.7	2.9	
Alutu	3.8	0.2	19		−0.8	2.1	
Haledebi	5.8	1.3	4.5		0.4	2.1	

3.2.2. Deformation Characteristics

Four of the volcanoes are best fit by a linear model: Dallol, Paka, Gada Ale and Dabbahu (Table 2 and Figure 6a,b). Although the sigmoidal model was preferred at Corbetti, Alu-Dallafilla and Silali, $|\Delta AIC|$was small (<10) and τ was large (461, 557 and 281 days, respectively), and we classify these as linear too (Figure 6c). For the seven steady deformation signals detected, velocities range from −3.2 to 4.6 cm/yr with most of the cases showing slow subsidence (Table 2). Steady uplift over the 5-year time period was

only reported at two volcanoes, Corbetti and Dabbahu, where sustained uplift has been attributed to a combination of magma movement and a viscoelastic rheology [44,45].

The sigmoidal model is preferred for six volcanoes: Fentale, Suswa, Erta Ale, Tullu Moje, Olkaria and Kone, but there is significant variation in the time-scale of the deformation episodes (Figure 6d,i). For Fentale, Suswa and Erta Ale, the characteristic time τ is smaller than 0.5 year with values of one month and half, two months and five months, respectively (Table 2). For Fentale, the time series shows a ramp increase with U_{max} = 8.3 cm in March 2015. For Suswa, the time series show a ramp increase with U_{max} = 6.2 cm with the onset of deformation starting around June 2018. For Tullu Moje, Olkaria and Kone, the characteristic time τ is larger than 0.5 year with values of 0.6 year, 0.7 year and 1.2 years, respectively (Table 2). Both Tullu Moje and Olkaria show an exponential decay trend, with LOS cumulative displacements of $\sim$15 cm and $\sim-$8 cm, respectively. Based on the sigmoid fit, the ground deformation started in early June 2015 for Olkaria and late September 2015 for Tullu Moje.

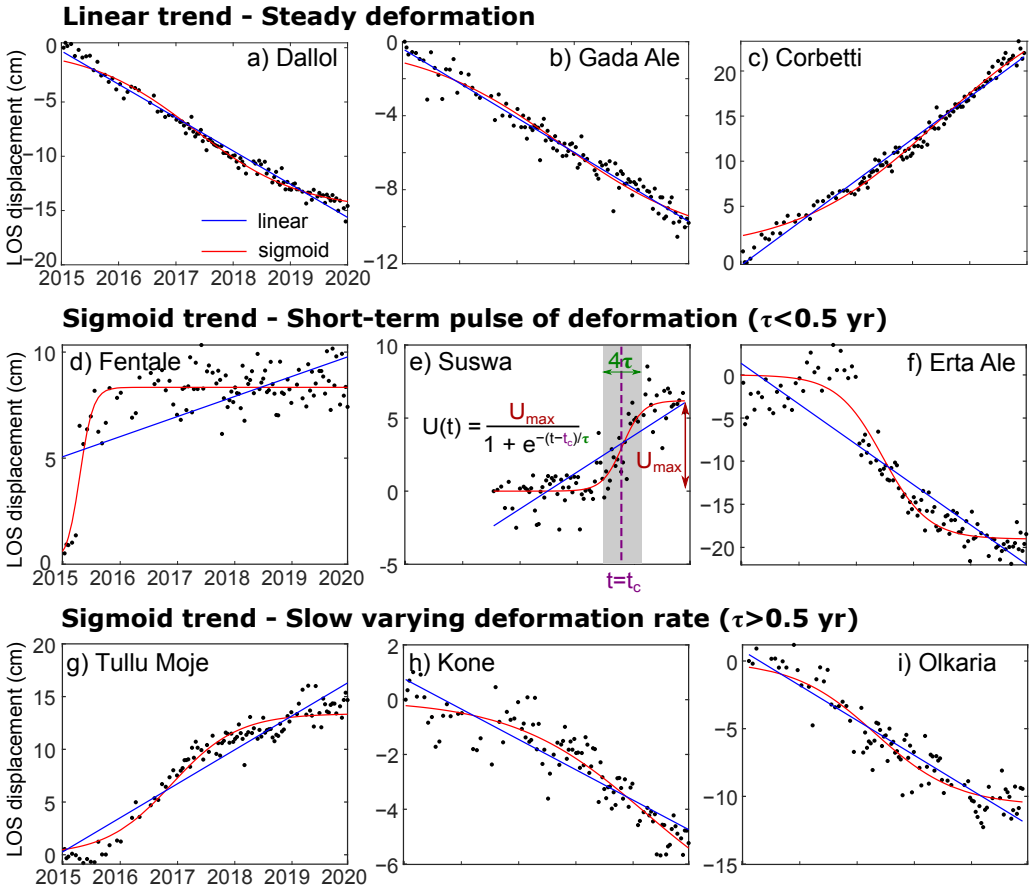

Figure 6. Examples of nine time series of LOS displacement showing the fit for the two functions: linear (blue) and sigmoid (red). Linear trend is preferred for the volcanoes (**a**) Dallol, (**b**) Gada Ale, and (**c**) Corbetti whereas sigmoid trend best fit for (**d**) Fentale, (**e**) Suswa, (**f**) Erta Ale, (**g**) Tullu Moje, (**h**) Kone and (**i**) Olkaria.

Three volcanoes (Nabro, Alutu and Haledebi) do not fit either the linear or sigmoidal models ($R^2 < 0.5$). All three can be described by a linear model superimposed with a seasonal signal (Figure S5 in Supplementary Materials). The amplitude of the seasonal signal, A_s, is $\sim$3 cm for Nabro and $\sim$2 cm for Alutu and Haledebi (Table 2).

3.3. Velocity Uncertainties

For the seven volcanoes whose time-series were classified as linear deformation (Corbetti, Alu-Dallafilla, Silali, Dallol, Paka, Gada Ale and Dabbahu), we estimate the LOS velocity uncertainties at the point B. In each case, the standard deviation of the velocity, σ_v, decreases linearly with the duration of time series Δt in a log-log plot (Figure 7). This indicates a power-law relationship: $\sigma_v = a\Delta t^{-b}$, in which a corresponds to the LOS velocity uncertainties after a 1-year period, and b corresponds to the decay rate. The value $b = 1$ is an indication of flicker noise (correlated), whereas $b = \frac{3}{2}$ indicates pure white noise (uncorrelated). After 5 years, LOS velocity uncertainties range from 0.05 cm/yr at Silali to 0.2 cm/yr at Dabbahu with an average value of 0.1 cm/yr and the decay rate b ranges from 1.35–1.65 with an average value of 1.5. These results indicate (1) a typical detection threshold of ∼1 mm/yr for EARS volcanoes based on 5 years of Sentinel-1 data and (2) that the velocity uncertainties in the Sentinel-1 time series are dominated by uncorrelated noise in agreement with previous InSAR studies [3,43].

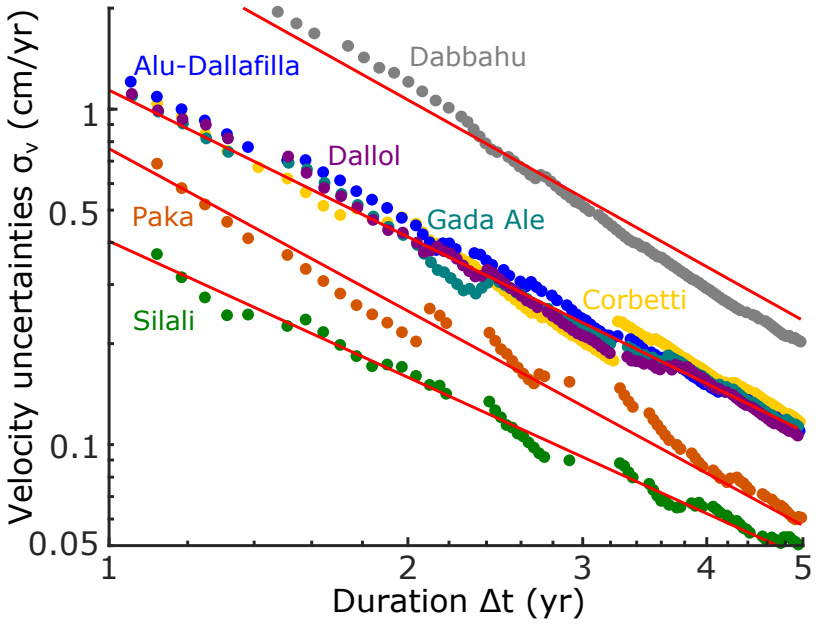

Figure 7. LOS velocity uncertainties σ_v as a function of the duration of the InSAR time series Δt (log-log scale) for the seven volcanoes showing persistent linear displacements for the period 2015–2020: Dabbahu, Alu-Dallafilla, Dallol, Gada Ale, Corbetti, Paka and Silali. Linear trends are an indication of a power-law relationship: $\sigma_v = a\Delta t^{-b}$, where a corresponds to the LOS velocity uncertainties after a 1-year period and b the decay rate (Table 2).

4. Discussion

4.1. Automated Detection Based on Signal-to-Noise Ratio

Based on our Sentinel-1 survey, the average temporal noise at EARS volcanoes, σ_A, is $\sim 1.35 \pm 0.5$ cm, with little systematic variation between regions. Using a threshold of $3\sigma_A$ (∼4 cm), we detected all the ground deformation signals reported by the manual study of Albino and Biggs [9], and in fact detected two previously unreported signals at Paka and Silali volcanoes (see Section 4.3). However, subtle signals with small amplitudes could still be missed (false negatives).

A threshold of 2σ (∼3 cm) is able to detect smaller signals, but a number of false positives can occur (Figure 5). In our study, there were five volcanoes with $2\sigma < |A_B| < 3\sigma$ after 5-years: Ma Alalta, Adwa and Ayelu in Afar, O'a caldera in the MER and Longonot in Kenya. None of these were reported by the study of Albino and Biggs [9].

- At Adwa and Ayelu, the velocities recorded at point B are 0.1 cm/yr, which is in the same order of magnitude as our estimates of LOS velocity uncertainties. In addition, part of the signal is correlated with topography, which suggests tropospheric residuals signals.
- At O'a caldera, the phase information is very sparse as the volcanic area is covered by three lakes (Shala, Abijata and Langano). Ground displacements has been only retrieved at the caldera rim and LOS velocities do not exceed 0.2 cm/yr. No clear deformation signal has been observed.
- At Longonot, the temporal noise is ∼2 cm, which is larger than the mean value calculated for the EARS. The signal detected has a long wavelength, and it can be observed in the entire scene (50 × 50 km), with LOS rates of displacement ranging from 0.5 cm/yr in the NW to −0.5 cm/yr in the SE. This pattern may suggest residual orbital ramps.
- At Ma Alalta, the signal is located on Quaternary rhyolite lava flows [46]. The maximum rate of LOS displacement is about −0.7 cm/yr, which is larger than the four cases previously described. Therefore, it is difficult to determine if this signal is noise or real ground deformation associated with the compaction or remobilization of volcanic products as previously observed in Kone lava flow [9].

In the framework of an automatic detection system, we recommend the use of a lower detection threshold (e.g., 2σ for the EARS) and re-evaluating positive results based on an expert analysis to identify potential false positives.

4.2. Previously Unreported Deformation

For two of the volcanoes with a high signal-to-noise ratio, Paka and Silali, no deformation has previously been reported in the Sentinel dataset (2015–2020). However, both experienced deformation during the Envisat era (2006–2010) [7,47,48]. At Paka, five distinct phases of unrest were identified with surface LOS displacement rates between 95 ± 1.3 cm/yr (July–August 2006) and 2.5 ± 0.9 cm/yr (February 2008–July 2010) [47]. Based on the modelling of ground deformation, unrest phases have been interpreted as the inflation and deflation of four simple sources located beneath the northeastern and southern flanks of the volcano at depths between 1 and 5 km. At Silali, a long-term linear subsidence signal with maximum LOS displacement rates of 1.6 ± 0.4 cm/yr was detected between October 2003 and September 2010, and modelled by the deflation of a source located at 4–5 km depth below the caldera [47].

For the period 2015–2020, $|A_B|/\sigma_A = 8.8$ at Paka and $|A_B|/\sigma_A = 8.5$ at Silali. Both timeseries were classified as linear, and the maximum LOS displacement rate was -0.7 ± 0.1 cm/yr (Figure 8b,e) at both. This rate is much smaller than observed during 2006–2010 but significantly greater than the uncertainty. The signals both show that LOS range increases in the same area as the previously detected signals (Figure 8), which is suggestive of long-term subsidence associated with magmatic or hydrothermal processes [49]. However, the profiles of displacements also show some similarity with the topography of the edifice (Figure 8c,f), which is typical of stratified atmospheric signals. Phase elevation corrections have already been applied at both of these volcanoes (see Section 3.1), but we cannot rule out that the signal may be the result of residual tropospheric signals instead of ground deformation.

4.3. Deformation Classification

We automatically classify the time-series associated with positive detections as 'linear' or 'sigmoidal' using Akaike's Information Criterion to chose the most appropriate functional form. Although, there were three signals that did not fit either the linear or sigmoidal models (Alutu, Haledebi and Nabro); these were well fit by a 'hybrid' model combining linear and seasonal models (Figure 9). Albino and Biggs [9] noted the seasonal signals at both Alutu and Haledebi and showed that they correlated with rainfall. The linear rate estimated for Nabro of 1.7 cm/yr (Table 2) is comparable to the 1.5 ± 0.5 cm/yr estimate of

Albino and Biggs [9]. Thus, the scheme could be easily improved by including an additional functional form to represent seasonal patterns combined with underlying deformation sources, e.g., [50].

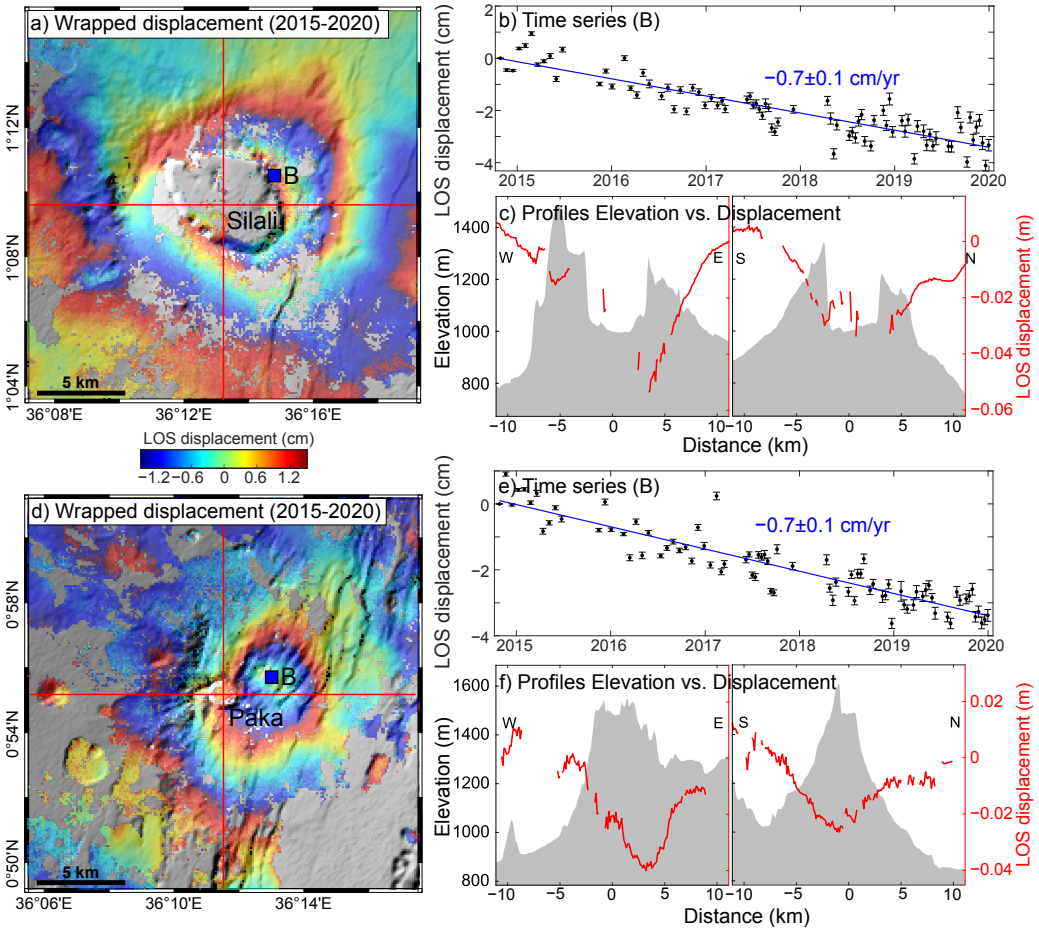

Figure 8. LOS displacement detected at the two Kenyan volcanoes, (**a**–**c**) Silali and (**d**–**f**) Paka, (**a**,**d**) wrapped cumulative displacements (LOS) for the 5-year time period (2015–2020), (**b**,**e**) time series of LOS displacements at the location B, (**c**,**f**) comparison between the profiles of displacements (red lines) and the topography (shaded area) along W-E (left) and S-N (right) directions.

However, the categories provided by the empirical time-series fits do not directly correspond with the process-based categories of Albino and Biggs [9]. The 'sigmoidal' classification represents a range of processes: the signals at Fentale and Erta Ale have been attributed to dyke intrusions [51,52], while Suswa, Tullu Moje and Olkaria are considered to be restless calderas [7]. For Erta Ale, the sigmoid fit is poorer than for the other cases (Figure 9), as the time series shows a complex trend: (1) a step-like LOS decrease of ∼10 cm on January 2017 associated with co-eruptive processes [51,53] followed by (2) a slow decay in displacement rate related to post-eruptive processes [54].

Similarly, the processes responsible for the five examples of linear subsidence are varied (Figure 9). The subsidence at Alu-Dalafilla and Dallol are thought to be long-term responses to recent activity: Alu-Dalafilla last erupted in 2008 [55] and there was a dike intrusion at Dallol in 2004 [56]. In contrast, Paka and Silali are restless calderas, with no recent activity [7]. The signal at Gada Ale has previously been attributed to poro-elastic fluid effects [9].

Although the spatial pattern of deformation can be used to discriminate between source processes with different geometries, many of the deformation signals are radially symmetrical. Thus, while empirical fitting can be useful for a first order categorisation of the

InSAR dataset, it cannot be used to uniquely determine the magmatic processes. Additional information from other monitoring streams, e.g., [57,58] or baseline knowledge of the long-term deformation patterns or eruptive history is needed for monitoring purposes.

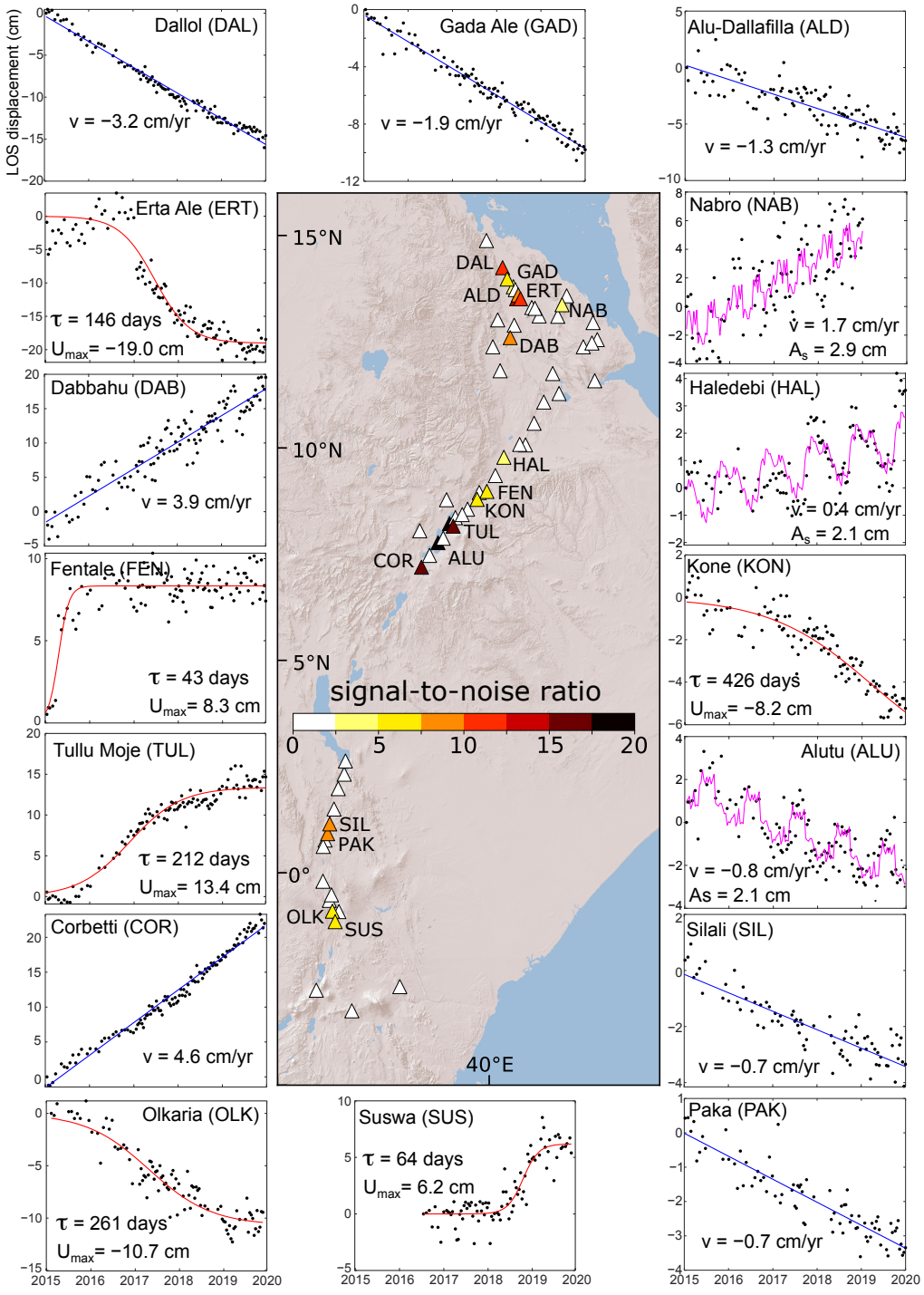

Figure 9. Map showing the ratio between the amplitude of the cumulative displacements and the temporal noise for the 64 EARS volcanoes analysed. Deformation signals are automatically detected for 16 volcanoes having a ratio exceeding 3 (colour triangles). Small panels show individual time series of LOS displacements for each deformed volcano in which temporal evolution is fitted either by linear (blue), sigmoid (red) or seasonal (pink) functions.

4.4. Measurement Uncertainty

The uncertainties on InSAR time series are the combination of several different processes: atmospheric noise, orbit and DEM uncertainties, errors in phase unwrapping and temporal decorrelation [59–62]. Our InSAR regional survey enables us to discuss various measures of uncertainty at the regional scale and to compare to other geographical environments.

For the EARS, interferograms from the majority of the volcanoes (∼75%) had a low phase-elevation correlation and did not require atmospheric corrections. Given that most EARS volcanoes have low relief (<1000 m), this is consistent with previous studies that have shown atmospheric uncertainty increases with volcano height, e.g., [28]. The only volcanoes at which atmospheric corrections were considered necessary (CDF(R^2 = 0.5) < 0.8) were high and/or large edifices (e.g., Silali and Paka) and volcanic systems located at the margin of the rift (e.g., Alid, Dubi, Butajiri), where the high relief is associated with the rift border faults rather than the volcanic edifice itself.

4.4.1. Regional Detection Threshold

InSAR measurement accuracy can be evaluated by the detection threshold defined as the minimum velocity that can be detected in the time series. This can be evaluated by calculating the noise δ of N independent interferograms or the noise of interferogram stacking with $v_{limit} = \frac{\delta_{ifg}\sqrt{N}}{t} = \frac{\delta_{stack}}{t}$, e.g., [4,59]. The detection threshold largely decreases with the duration of the time series and is highly dependent on the content of atmospheric noise. Assuming that the noise is characterised by the value of $2\sigma_A$, the detection threshold can be expressed as $v_{limit} = \frac{2\sigma_A}{t}$.

Therefore, the average detection threshold in the East African Rift System is 0.5–0.6 cm/yr for a 5-year duration. For volcanoes in Central Andes, Pritchard and Simons [63] found a detection threshold of 0.4 cm/yr for a 5-year ERS-1/2 (C-band) time series, assuming a maximum error of 2 cm per interferogram. Thus, our estimates of the detection threshold in the EARS are in good agreement with previous ones found for Central Andes volcanoes. We may conclude that, for C-band sensors, the limit of detection is 0.4–0.6 cm/yr for volcanoes located in arid or semi-arid environment (high coherence and low atmospheric noise), such as the EARS and Central Andes.

In comparison, [20] estimated the average detection threshold for a set of 20 volcanoes in Central America to be 2.4 cm/yr using a 3-year time-series of ALOS-PALSAR (L-band) data, equivalent to 1.4 cm/yr for a 5-year duration. Such results are three times higher than our estimates. Discrepancies are due to the tropical environment of Central America (low coherence and high atmospheric noise) as well as the difference in radar wavelength. Indeed, long wavelength sensors such as L-band are less sensitive to detecting small displacements.

4.4.2. Velocity Errors for Long-Term Signals

Analysis of the persistent linear trend at seven EARS volcanoes shows that velocity uncertainties are inversely proportional to the duration of the time series. For the 5-year observation period, the typical LOS velocity uncertainty in the EARS was ∼0.1 cm/yr and related to uncorrelated noise, that is consistent with results from two previous Sentinel-1 studies conducted in Japan and Turkey [3,43]. Our results are also in good agreement with theoretical simulations, looking at the effect of tropospheric delays, which demonstrates that a detection level of 0.1 cm/yr can be achieved for Sentinel-1 time series having regularly sampled data for a period longer than 5 years [64].

Small phase biases due to the variation in scattering properties of sub-resolution scatterers caused by moisture changes and vegetation growth can propagate through time series of multi-looked interferograms causing a significant bias in velocity maps [65–67]. Although the EARS is mostly arid and sparsely vegetated, this effect could explain some of the uncertainties in our velocity estimates, particularly for volcanoes with multiple land cover types as the impact of the phase errors varies across the scene.

Most InSAR studies do not explicitly consider the choice of reference frame as a source of uncertainty. Here, we demonstrate that this choice is not trivial and can induce variations up to 1 cm/yr on the LOS velocity derived. From our study, we show that the average error is ∼0.5 cm/yr for the EARS, which is five times larger than the errors associated with noise. Therefore, the use of an external dataset (e.g., GNSS data) for referencing Sentinel-1, e.g., [3,45], is crucial to be able to study strain accumulation and partitioning in the EARS, where extension rates range from ∼2 mm/yr in Malawi to ∼6 mm/yr in the Main Ethiopian Rift [68].

5. Conclusions

Here, we provide a framework to produce routinely Sentinel-1 InSAR time series of displacements from LiCSAR products that is adapted to semi-arid volcanic environment. We apply our methodology to the EARS for the period 2015–2020. Among the 64 volcanic centres, sixteen show large signal-to-noise ratio with the amplitude of the cumulative displacements exceeding three times the temporal noise of the time series (Figure 9).

By performing a regional statistical analysis of the time series, we found that the average limit of detection in the EARS region is around 3 cm (2σ). Therefore, we expect to detect linear trend with rates larger than 0.5 cm/yr with an uncertainty of 0.1 cm/yr after a 5-year period.

We automatically classify the deformation signals as 'linear', 'sigmoidal' or 'hybrid'. Although this classification in three classes does not reflect the diversity of magmatic processes, the automatic fitting provides an easy way to discriminate between steady deformation (linear), slowly varying deformation rate (large sigmoid with $\tau > 0.5$ yr) and short-term pulses of deformation (tight sigmoid with $\tau < 0.5$ yr). Such information can be used during real-time monitoring to detect anomalies in the time series by comparing the "real" ground displacements with the "predicted" displacements derived from the trend.

Supplementary Materials: The following supporting information can be downloaded at: https://www.mdpi.com/article/10.3390/rs14225703/s1. Table S1: List of the 30 volcanoes processed in the Afar region. For each of them, we indicate the latitude, the longitude, the mean coherence, the phase-elevation correlation and the velocity uncertainty due to the selection of the reference point. Table S2: List of the 16 volcanoes processed in the Main Ethiopian Rift. For each of them, we indicate the latitude, the longitude, the mean coherence, the phase-elevation correlation and the velocity uncertainty due to the selection of the reference point. Table S3: List of the 17 volcanoes processed in the Kenya-Tanzania rift. For each of them, we indicate the latitude, the longitude, the mean coherence, the phase-elevation correlation and the velocity uncertainty due to the selection of the reference point. Figure S1: Quality check of LiCSAR products over Fentale volcano. For each interferogram, we plot the mean coherence (blue crosses) and the fraction of unwrapped pixels (red crosses). Among the 294 interferograms processed, six of them have values much lower than the common trend (yellow circles). Figure S2: Number of interferograms processed per volcano for the three regions: (a) Afar, (b) MER and (c) Kenya-Tanzania. Blue and red bars indicate the proportion of interferograms selected and rejected, respectively. The selection is based on the two criteria, mean coherence and fraction of unwrapped pixels, as described in Figure S1. Figure S3: Boxplots of the elevation for each volcanic area processed ($0.5^\circ \times 0.5^\circ$) for (a) Afar, (b) MER and (c) Kenya-Tanzania. Dashed lines show the range of elevation (between the minimum and maximum values) and blue rectangles indicate the interquartile range (between 25th and 75th percentiles). Red vertical lines correspond to the median elevation and black triangles indicate the maximum elevation of the volcanic edifice. Numbers in brackets indicate the volcano's height evaluated as the difference between the median value and the edifice's elevation. Figure S4: Examples of automated time series produced for (a–c) three non-deformed volcanoes: Adwa, Gedamsa and Korosi and (d–f) three deformed volcanoes: Kone, Olkaria and Tullu Moje. Black and red dots show the time series for the point A (baseline in non volcanic area) and the point B (signal in the volcanic area), respectively. The temporal standard deviation of the baseline (σ_A) characterises the level of noise whereas the magnitude of the cumulative displacement ($|A_B|$) characterises the amplitude of the signal. Figure S5: Seasonnal signals superposed to linear trend observed in the volcanoes (a) Nabro, (b) Alutu and (c) Haledebi.

Author Contributions: Conceptualization, F.A. and J.B.; methodology, F.A.; software, M.L. and Y.M.; formal analysis, F.A.; investigation, F.A.; resources, J.B.; data curation, M.L. and Y.M.; writing—original draft preparation, F.A.; writing—review and editing, J.B., M.L. and Y.M.; visualization, F.A.; supervision, J.B.; project administration, J.B.; funding acquisition, J.B. All authors have read and agreed to the published version of the manuscript.

Funding: J.B. and F.A. were funded by the NERC Large Grant RiftVolc (NE/L013649/1), the NERC innovation grant—Making Satellite Volcano Deformation Analysis Accessible (NE/S013970/1)—and supported by the NERC Centre for the Observation and Modeling of Earthquakes, Volcanoes, and Tectonics (COMET, http://comet.nerc.ac.uk, accessed on 25 October 2022), a partnership between UK Universities and the British Geological Survey. F.A. is part of Labex OSUG@2020 (ANR10 LABX56). J.B. was supported by a Leverhulme Prize (PLP-2018-362) and received funding from the European Research Council (ERC) under the European Union's Horizon 2020 research and innovation programme (MAST; Grant No. 101003173 and DEEPVOLC; Grant No. 866085).

Data Availability Statement: Sentinel-1 InSAR products processed by LiCSAR are available on the Centre for Environmental Data Analysis (CEDA) archive (http://data.ceda.ac.uk/neodc/comet/data/licsar_products, accessed on 25 October 2022). The cropped products and the time series of displacements for each volcano were archived with the NERC's National Geoscience Data Centre (NGDC) and available online (https://doi.org/10.5285/e7c3177b-4c73-4c20-961f-03afd09ccf69, accessed on 25 October 2022).

Acknowledgments: We thank Nantheera Anantrasirichai and Matthew Gaddes for useful discussions. We thank the three anonymous reviewers for their useful comments, which improved the manuscript.

Conflicts of Interest: The authors declare no conflict of interest. The funders had no role in the design of the study; in the collection, analyses, or interpretation of data; in the writing of the manuscript; or in the decision to publish the results.

References

1. Wang, H.; Wright, T.J.; Liu-Zeng, J.; Peng, L. Strain Rate Distribution in South-Central Tibet From Two Decades of InSAR and GPS. *Geophys. Res. Lett.* **2019**, *46*, 5170–5179. [CrossRef]
2. Walters, R.; Holley, R.; Parsons, B.; Wright, T. Interseismic strain accumulation across the North Anatolian Fault from Envisat InSAR measurements. *Geophys. Res. Lett.* **2011**, *38*. [CrossRef]
3. Weiss, J.R.; Walters, R.J.; Morishita, Y.; Wright, T.J.; Lazecky, M.; Wang, H.; Hussain, E.; Hooper, A.J.; Elliott, J.R.; Rollins, C.; et al. High-resolution surface velocities and strain for Anatolia from Sentinel-1 InSAR and GNSS data. *Geophys. Res. Lett.* **2020**, *47*, e2020GL087376. [CrossRef]
4. Ebmeier, S.; Biggs, J.; Mather, T.; Amelung, F. On the lack of InSAR observations of magmatic deformation at Central American volcanoes. *J. Geophys. Res. Solid Earth* **2013**, *118*, 2571–2585. [CrossRef]
5. Pritchard, M.E.; Simons, M. A satellite geodetic survey of large-scale deformation of volcanic centres in the central Andes. *Nature* **2002**, *418*, 167–171. [CrossRef]
6. Chaussard, E.; Amelung, F. Precursory inflation of shallow magma reservoirs at west Sunda volcanoes detected by InSAR. *Geophys. Res. Lett.* **2012**, *39*. [CrossRef]
7. Biggs, J.; Anthony, E.; Ebinger, C. Multiple inflation and deflation events at Kenyan volcanoes, East African Rift. *Geology* **2009**, *37*, 979–982. [CrossRef]
8. Biggs, J.; Bastow, I.; Keir, D.; Lewi, E. Pulses of deformation reveal frequently recurring shallow magmatic activity beneath the Main Ethiopian Rift. *Geochem. Geophys. Geosystems* **2011**, *12*. [CrossRef]
9. Albino, F.; Biggs, J. Magmatic Processes in the East African Rift System: Insights from a 2015-2020 Sentinel-1 InSAR survey. *Geochem. Geophys. Geosystems* **2021**, *22*, e2020GC009488. [CrossRef]
10. Raspini, F.; Bianchini, S.; Ciampalini, A.; Del Soldato, M.; Solari, L.; Novali, F.; Del Conte, S.; Rucci, A.; Ferretti, A.; Casagli, N. Continuous, semi-automatic monitoring of ground deformation using Sentinel-1 satellites. *Sci. Rep.* **2018**, *8*, 7253. [CrossRef]
11. Biggs, J.; Wright, T.J. How satellite InSAR has grown from opportunistic science to routine monitoring over the last decade. *Nat. Commun.* **2020**, *11*, 3863. [CrossRef] [PubMed]
12. Agram, P.; Owen, S.; Hua, H.; Manipon, G.; Sacco, G.; Bue, B.; Fielding, E.; Yun, S.; Simons, M.; Webb, F.; et al. ARIA: Delivering state-of-the-art InSAR products to end users. In Proceedings of the AGU Fall Meeting Abstracts, San Francisco, CA, USA, 12–16 December 2016; Volume 2016, p. G33C-02.
13. Meyer, F.J.; Whitley, M.; Logan, T.; McAlpin, D.B.; Hogenson, K.; Nicoll, J.B. The Sarviews Project: Automated Processing Of Sentinel-1 Sar Data For Geoscience And Hazard Response. In Proceedings of the IGARSS 2019—2019 IEEE International Geoscience and Remote Sensing Symposium, Yokohama, Japan, 28 July–2 August 2019; pp. 5468–5471.

14. Foumelis, M.; Papadopoulou, T.; Bally, P.; Pacini, F.; Provost, F.; Patruno, J. Monitoring Geohazards Using On-Demand and Systematic Services On Esa's Geohazards Exploitation Platform. In Proceedings of the IGARSS 2019—2019 IEEE International Geoscience and Remote Sensing Symposium, Yokohama, Japan, 28 July–2 August 2019; pp. 5457–5460.
15. Lazecký, M.; Spaans, K.; González, P.J.; Maghsoudi, Y.; Morishita, Y.; Albino, F.; Elliott, J.; Greenall, N.; Hatton, E.; Hooper, A.; et al. LiCSAR: An automatic InSAR tool for measuring and monitoring tectonic and volcanic activity. *Remote Sens.* **2020**, *12*, 2430. [CrossRef]
16. Global Volcanism Program. *Volcanoes of the World*; Venzke, E., Ed.; Smithsonian Institution: Washington, DC, USA, 2013.
17. Brown, S.K.; Auker, M.; Sparks, R. Populations around Holocene volcanoes and development of a Population Exposure Index. In *Global Volcanic Hazards and Risk*; Cambridge University Press: Cambridge, UK, 2015; pp. 223–232.
18. Hanssen, R.F. *Radar Interferometry: Data Interpretation and Error Analysis*; Springer Science & Business Media: Berlin/Heidelberg, Germany, 2001; Volume 2.
19. Werner, C.; Wegmüller, U.; Strozzi, T.; Wiesmann, A. Gamma SAR and interferometric processing software. In Proceedings of the Ers-Envisat Symposium, Gothenburg, Sweden, 16–20 October 2000; Volume 1620, p. 1620.
20. Ebmeier, S.; Biggs, J.; Mather, T.; Amelung, F. Applicability of InSAR to tropical volcanoes: Insights from Central America. *Geol. Soc. Lond. Spec. Publ.* **2013**, *380*, 15–37. [CrossRef]
21. Yip, S.T.H.; Biggs, J.; Albino, F. Reevaluating Volcanic Deformation Using Atmospheric Corrections: Implications for the Magmatic System of Agung Volcano, Indonesia. *Geophys. Res. Lett.* **2019**, *46*, 13704–13711. [CrossRef]
22. Albino, F.; Biggs, J.; Yu, C.; Li, Z. Automated Methods for Detecting Volcanic Deformation Using Sentinel-1 InSAR Time Series Illustrated by the 2017–2018 Unrest at Agung, Indonesia. *J. Geophys. Res. Solid Earth* **2020**, *125*, e2019JB017908. [CrossRef]
23. Beauducel, F.; Briole, P.; Froger, J.L. Volcano-wide fringes in ERS synthetic aperture radar interferograms of Etna (1992–1998): Deformation or tropospheric effect? *J. Geophys. Res. Solid Earth* **2000**, *105*, 16391–16402. [CrossRef]
24. Biggs, J.; Dogru, F.; Dagliyar, A.; Albino, F.; Yip, S.; Brown, S.; Anantrasirichai, N.; Atıcı, G. Baseline monitoring of volcanic regions with little recent activity: application of Sentinel-1 InSAR to Turkish volcanoes. *J. Appl. Volcanol.* **2021**, *10*, 2. [CrossRef]
25. Delacourt, C.; Briole, P.; Achache, J. Tropospheric corrections of SAR interferograms with strong topography. Application to Etna. *Geophys. Res. Lett.* **1998**, *25*, 2849–2852. [CrossRef]
26. Remy, D.; Bonvalot, S.; Briole, P.; Murakami, M. Accurate measurements of tropospheric effects in volcanic areas from SAR interferometry data: Application to Sakurajima volcano (Japan). *Earth Planet. Sci. Lett.* **2003**, *213*, 299–310. [CrossRef]
27. Pinel, V.; Hooper, A.; De la Cruz-Reyna, S.; Reyes-Davila, G.; Doin, M.; Bascou, P. The challenging retrieval of the displacement field from InSAR data for andesitic stratovolcanoes: Case study of Popocatepetl and Colima Volcano, Mexico. *J. Volcanol. Geotherm. Res.* **2011**, *200*, 49–61. [CrossRef]
28. Parker, A.L.; Biggs, J.; Walters, R.J.; Ebmeier, S.; Wright, T.J.; Teanby, N.A.; Lu, Z. Systematic assessment of atmospheric uncertainties for InSAR data at volcanic arcs using large-scale atmospheric models: Application to the Cascade volcanoes, United States. *Remote Sens. Environ.* **2015**, *170*, 102–114. [CrossRef]
29. Bekaert, D.; Walters, R.; Wright, T.; Hooper, A.; Parker, D. Statistical comparison of InSAR tropospheric correction techniques. *Remote Sens. Environ.* **2015**, *170*, 40–47. [CrossRef]
30. Stephens, K.J.; Wauthier, C.; Bussard, R.C.; Higgins, M.; LaFemina, P.C. Assessment of Mitigation Strategies for Tropospheric Phase Contributions to InSAR Time-Series Datasets over Two Nicaraguan Volcanoes. *Remote Sens.* **2020**, *12*, 782. [CrossRef]
31. Beck, H.E.; Zimmermann, N.E.; McVicar, T.R.; Vergopolan, N.; Berg, A.; Wood, E.F. Present and future Köppen-Geiger climate classification maps at 1-km resolution. *Sci. Data* **2018**, *5*, 180214. [CrossRef]
32. Biggs, J.; Amelung, F.; Gourmelen, N.; Dixon, T.H.; Kim, S.W. InSAR observations of 2007 Tanzania rifting episode reveal mixed fault and dyke extension in an immature continental rift. *Geophys. J. Int.* **2009**, *179*, 549–558. [CrossRef]
33. Pagli, C.; Wang, H.; Wright, T.J.; Calais, E.; Lewi, E. Current plate boundary deformation of the Afar rift from a 3-D velocity field inversion of InSAR and GPS. *J. Geophys. Res. Solid Earth* **2014**, *119*, 8562–8575. [CrossRef]
34. Doubre, C.; Deprez, A.; Masson, F.; Socquet, A.; Lewi, E.; Grandin, R.; Nercessian, A.; Ulrich, P.; De Chabalier, J.B.; Saad, I.; et al. Current deformation in Central Afar and triple junction kinematics deduced from GPS and InSAR measurements. *Geophys. J. Int.* **2017**, *208*, 936–953. [CrossRef]
35. Schmidt, D.A.; Bürgmann, R. Time-dependent land uplift and subsidence in the Santa Clara valley, California, from a large interferometric synthetic aperture radar data set. *J. Geophys. Res. Solid Earth* **2003**, *108*. [CrossRef]
36. Finnegan, N.J.; Pritchard, M.E.; Lohman, R.B.; Lundgren, P.R. Constraints on surface deformation in the Seattle, WA, urban corridor from satellite radar interferometry time-series analysis. *Geophys. J. Int.* **2008**, *174*, 29–41. [CrossRef]
37. Usai, S. A least squares database approach for SAR interferometric data. *IEEE Trans. Geosci. Remote Sens.* **2003**, *41*, 753–760. [CrossRef]
38. Akaike, H. A new look at the statistical model identification. *IEEE Trans. Autom. Control* **1974**, *19*, 716–723. [CrossRef]
39. Efron, B.; Tibshirani, R. Bootstrap methods for standard errors, confidence intervals, and other measures of statistical accuracy. *Stat. Sci.* **1986**, *1*, 54–75. [CrossRef]
40. Zhang, J.; Bock, Y.; Johnson, H.; Fang, P.; Williams, S.; Genrich, J.; Wdowinski, S.; Behr, J. Southern California Permanent GPS Geodetic Array: Error analysis of daily position estimates and site velocities. *J. Geophys. Res. Solid Earth* **1997**, *102*, 18035–18055. [CrossRef]

41. Mao, A.; Harrison, C.G.; Dixon, T.H. Noise in GPS coordinate time series. *J. Geophys. Res. Solid Earth* **1999**, *104*, 2797–2816. [CrossRef]
42. Santamaría-Gómez, A.; Bouin, M.N.; Collilieux, X.; Wöppelmann, G. Correlated errors in GPS position time series: Implications for velocity estimates. *J. Geophys. Res. Solid Earth* **2011**, *116*. [CrossRef]
43. Morishita, Y.; Lazecky, M.; Wright, T.J.; Weiss, J.R.; Elliott, J.R.; Hooper, A. LiCSBAS: An Open-Source InSAR Time Series Analysis Package Integrated with the LiCSAR Automated Sentinel-1 InSAR Processor. *Remote Sens.* **2020**, *12*, 424. [CrossRef]
44. Gottsmann, J.; Biggs, J.; Lloyd, R.; Biranhu, Y.; Lewi, E. Ductility and compressibility accommodate high magma flux beneath a silicic continental rift caldera: Insights from Corbetti caldera (Ethiopia). *Geochem. Geophys. Geosystems* **2020**, *21*, e2020GC008952. [CrossRef]
45. Moore, C.; Wright, T.; Hooper, A. Rift Focusing and Magmatism During Late-Stage Rifting in Afar. *J. Geophys. Res. Solid Earth* **2021**, *126*, e2020JB021542. [CrossRef]
46. Wiart, P.; Oppenheimer, C. Large magnitude silicic volcanism in north Afar: The Nabro Volcanic Range and Ma'alalta volcano. *Bull. Volcanol.* **2005**, *67*, 99–115. [CrossRef]
47. Biggs, J.; Robertson, E.; Cashman, K. The lateral extent of volcanic interactions during unrest and eruption. *Nat. Geosci.* **2016**, *9*, 308–311. [CrossRef]
48. Robertson, E.A.M. Magma Storage and Transport at Kenyan Rift Volcanoes: A Remote Sensing Perspective. PhD Thesis, University of Bristol, Bristol, UK, 2015.
49. Caricchi, L.; Biggs, J.; Annen, C.; Ebmeier, S. The influence of cooling, crystallisation and re-melting on the interpretation of geodetic signals in volcanic systems. *Earth Planet. Sci. Lett.* **2014**, *388*, 166–174. [CrossRef]
50. Hill, P.; Biggs, J.; Ponce-López, V.; Bull, D. Time-Series Prediction Approaches to Forecasting Deformation in Sentinel-1 InSAR Data. *J. Geophys. Res. Solid Earth* **2021**, *126*, e2020JB020176. [CrossRef]
51. Moore, C.; Wright, T.; Hooper, A.; Biggs, J. The 2017 Eruption of Erta'Ale Volcano, Ethiopia: Insights Into the Shallow Axial Plumbing System of an Incipient Mid-Ocean Ridge. *Geochem. Geophys. Geosystems* **2019**, *20*, 5727–5743. [CrossRef]
52. Temtime, T.; Biggs, J.; Lewi, E.; Ayele, A. Evidence for Active Rhyolitic Dyke Intrusion in the Northern Main Ethiopian Rift from the 2015 Fentale Seismic Swarm. *Geochem. Geophys. Geosystems* **2020**, *21*, e2019GC008550. [CrossRef]
53. Xu, W.; Rivalta, E.; Li, X. Magmatic architecture within a rift segment: Articulate axial magma storage at Erta Ale volcano, Ethiopia. *Earth Planet. Sci. Lett.* **2017**, *476*, 79–86. [CrossRef]
54. Xu, W.; Xie, L.; Aoki, Y.; Rivalta, E.; Jónsson, S. Volcano-wide deformation after the 2017 Erta Ale dike intrusion, Ethiopia, observed with radar interferometry. *J. Geophys. Res. Solid Earth* **2020**, *125*, e2020JB019562. [CrossRef]
55. Pagli, C.; Wright, T.J.; Ebinger, C.J.; Yun, S.H.; Cann, J.R.; Barnie, T.; Ayele, A. Shallow axial magma chamber at the slow-spreading Erta Ale Ridge. *Nat. Geosci.* **2012**, *5*, 284–288. [CrossRef]
56. Nobile, A.; Pagli, C.; Keir, D.; Wright, T.J.; Ayele, A.; Ruch, J.; Acocella, V. Dike-fault interaction during the 2004 Dallol intrusion at the northern edge of the Erta Ale Ridge (Afar, Ethiopia). *Geophys. Res. Lett.* **2012**, *39*. [CrossRef]
57. Reath, K.; Pritchard, M.; Biggs, J.; Andrews, B.; Ebmeier, S.; Bagnardi, M.; Girona, T.; Lundgren, P.; Lopez, T.; Poland, M. Using conceptual models to relate multiparameter satellite data to subsurface volcanic processes in Latin America. *Geochem. Geophys. Geosystems* **2020**, *21*, e2019GC008494. [CrossRef]
58. Voight, B.; Sparks, R.; Miller, A.; Stewart, R.; Hoblitt, R.; Clarke, A.; Ewart, J.; Aspinall, W.; Baptie, B.; Calder, E.; et al. Magma flow instability and cyclic activity at Soufriere Hills volcano, Montserrat, British West Indies. *Science* **1999**, *283*, 1138–1142. [CrossRef]
59. Biggs, J.; Wright, T.; Lu, Z.; Parsons, B. Multi-interferogram method for measuring interseismic deformation: Denali Fault, Alaska. *Geophys. J. Int.* **2007**, *170*, 1165–1179. [CrossRef]
60. Fattahi, H.; Amelung, F. InSAR uncertainty due to orbital errors. *Geophys. J. Int.* **2014**, *199*, 549–560. [CrossRef]
61. Fattahi, H.; Amelung, F. InSAR bias and uncertainty due to the systematic and stochastic tropospheric delay. *J. Geophys. Res. Solid Earth* **2015**, *120*, 8758–8773. [CrossRef]
62. Fattahi, H.; Simons, M.; Agram, P. InSAR time-series estimation of the ionospheric phase delay: An extension of the split range-spectrum technique. *IEEE Trans. Geosci. Remote Sens.* **2017**, *55*, 5984–5996. [CrossRef]
63. Pritchard, M.; Simons, M. An InSAR-based survey of volcanic deformation in the central Andes. *Geochem. Geophys. Geosyst.* **2004**, *5*. [CrossRef]
64. Havazli, E.; Wdowinski, S. Detection threshold estimates for insar time series: A simulation of tropospheric delay approach. *Sensors* **2021**, *21*, 1124. [CrossRef] [PubMed]
65. De Zan, F.; Zonno, M.; Lopez-Dekker, P. Phase inconsistencies and multiple scattering in SAR interferometry. *IEEE Trans. Geosci. Remote Sens.* **2015**, *53*, 6608–6616. [CrossRef]
66. Ansari, H.; De Zan, F.; Parizzi, A. Systematic Interferometric Phase Biases and their Impact on Earth Surface Deformation Monitoring. In Proceedings of the EUSAR 2021; 13th European Conference on Synthetic Aperture Radar, Online, 29 March–1 April 2021; pp. 1–6.
67. Maghsoudi, Y.; Hooper, A.; Wright, T.J.; Ansari, H.; Lazecky, M. Characterizing and Correcting Phase Biases in Short-Term, Multilooked Interferograms. *Remote. Sens. Environ.* **2021**, *275*, 113022. [CrossRef]
68. Stamps, D.S.; Calais, E.; Saria, E.; Hartnady, C.; Nocquet, J.M.; Ebinger, C.J.; Fernandes, R.M. A kinematic model for the East African Rift. *Geophys. Res. Lett.* **2008**, *35*, L05304. [CrossRef]